Prototyping Integrity Monitors for PPP Fault Detections

Yu-Fang Lai, Juan Blanch, Todd Walter
Stanford University
Erin Kahr, Edmond Leahy, Pedro Silva, Cameron Ellum
NovAtel Inc.

BIOGRAPHY

Yu-Fang Lai is a Ph.D. candidate at Stanford GPS Lab. He received Bachelor's degree in Aero/Astro from National Cheng-Kung University in 2020, and Master's degree in Aero/Astro from Stanford in 2022.
Juan Blanch is a senior research engineer at Stanford University. He is a graduate of Ecole Polytechnique in France, he holds an M.S. degree in electrical engineering and a Ph.D. degree in aeronautics and astronautics from Stanford University.
Todd Walter is a Professor at Stanford University and the faculty of Stanford GPS Lab. He received his B.S. degree in physics from Rensselaer Polytechnic Institute and his Ph.D. degree in 1993 from Stanford University.

ABSTRACT

Precise Point Positioning (PPP) is a GNSS positioning technique that is capable of achieving centimeter-level accuracy. A PPP system consists of several reference stations to deliver precise corrections such as precise satellite clock bias and precise ephemeris for the users to minimize the errors. In addition for providing access to the PPP service (corrections), it is also important for the PPP system to ensure the integrity of the user is protected. In this paper, a fault-monitoring system prototype based on fault-tolerant PPP filters is proposed, that is capable of monitoring and detecting possible satellite clock fault in real-time operation for static receiver. Artificial and actual GPS clock faults on PRN-1 on Jan. 25^{th}, Jan. 28^{th} and July. 10^{th} are examined to verify the capability of the filter and the monitoring system. It is shown that the prototype system is able to detect and identify the faulted satellite from the real GPS measurement during the fault period, which indicates the capability of real-time operation for such monitor design.

I. INTRODUCTION

GNSS relies on measuring the pseudo-range between the user and the satellites to estimate the position of the user. Conventional positioning method formulates localization problem as least-square optimization problem that finding the best position that minimizes the pseudo-range errors. The result is predominately influenced by the uncertainties of the pseudo-range measurement, such as Ionospheric delay, Tropospheric delay, clock bias, clock drift, Doppler effect, Carrier Phase Ambiguities etc. Although sophisticated models have been developed to reduce the error of the positioning solution, the inherent uncertainties still exist and prohibit improving the accuracy of position estimation. Other techniques such as differential GPS, or Real-time Kinematic (RTK) can significantly reduce the error sources but requires additional reference stations and the users must remain contact with and be in the vicinity of the stations to receive corrections. The reference stations broadcast all the measurements are in view, including code and carrier phase, as well as their locations to the users to let them determine their relative position and ambiguities. The users then combine this information with the position from the station to remove any relative error source and obtain the absolute position of the user up to centimeter accuracy. On the other hand, Precise Point Positioning (PPP) does not require nearby reference stations and is still capable of achieving the centimeter-level accuracy as RTK. PPP performs state estimation in real-time with positions and error modelings as part of its state. It requires external precise corrections such as precise ephemeris, precise satellite clock bias, Antenna Phase Center (APC) Offset, Differential Code Bias (DCB) etc. Without the precise correction the accuracy of the filter will degrade and becomes so-called Single Point Positioning (SPP), with the position error reaches as large as $1\sim3$ m.

The connection to the correction information can be through either internet (Mervart et al., 2022) or satellite (Barrios et al., 2020). For safety critical applications of PPP, it will be necessary to ensure the integrity of the pseudorange measurements as received by the users (that is the combination of the broadcast GNSS clock and ephemeris and the PPP corrections). For PPP services intending to provide safety critical corrections, the reference stations will also need to monitor the integrity of corrections for the PPP users. The design of such a monitoring system will depend on the integrity and continuity requirements and on the threats that need to be mitigated (the threat model). As a result, it is a very complex undertaking.

In order to achieve centimeter-level accuracy for the PPP positioning, every part of the correction models and their implementations in the PPP filter must be correct and accurate. Sometimes challenging to find the cause of abnormal behavior of our newly

designed PPP filter, therefore we used GINav(Chen et al., 2021), which is an open-source and MATLAB-based GNSS/INS navigation system to serve as cross-validation in the development of the integrity PPP monitor in this paper.

In addition to providing correction messages to the user, the reference stations are also required to monitor the GNSS signals and take action in case of faults, such as satellite clock fault, occur. This is called detection and is the main purpose of this paper. The reference stations utilize the knowledge of the station and PPP estimation to ensure the integrity of the correction message being broadcast. In this paper, we develop a fault monitoring PPP filter based on Kalman Filter framework that is capable of detecting the usual GNSS signal faults such as constant and ramp satellite clock faults.

Ensuring the integrity of the GNSS user has always been a crucial task for GNSS receivers. Advanced Receiver Autonomous Integrity Monitoring (ARAIM) is a concept that include all GNSS constellations for the receiver to do Fault Detection and Exclusion (FDE) while only the GNSS measurements are available to the receiver. The baseline Solution Separation (SS) based ARAIM algorithm proposed in Blanch et al. (2015) provided the detail derivations of Alert Limit (AL) and Protection Level (PL) from snapshot solution that civil aviation needed to meet Federal Aviation Administration (FAA) requirements. The SS based protection level computation can also be used in PPP (Gunning et al., 2018), where a bank of filters are ran in parallel to perform SS protection level computation in static and kinetic scenarios. A similar strategy is applied by the integrity monitor proposed in this paper with a group of filters run in parallel and each of it detects different faults. The difference is the integrity monitor in this paper detects possible faults in the pesudorange domain while ARAIM in the position domain, which makes it more intuitive and straightforward than baseline ARAIM.

The majority of the GNSS faults occurred in the past are satellite clock faults. This is the type of fault the integrity monitor prototype monitors. Wang and Walter (2023) outlined the most recent GPS and Galileo anomalies. Among the GPS satellite clock faults are the step and ramp type occurred on PRN 1 on January 25, 2023 and on PRN 22 on October 2, 2022.

The goal of this paper is to start this task by developing a simple prototype of an integrity monitoring system for PPP. We will start by describing a list of the most likely threats that will need to be mitigated. This list will start with clock errors, or clock-like errors. For these threats, we propose a set of monitors based on fault-tolerant PPP filters that guarantee integrity.

II. IGS DATASET

The International GNSS Service, IGS (2023), has 515 GNSS receiver stations world-wide as of June 13th 2023 and it provides free access to varies GNSS products. The number of stations available may vary from days to days due to new stations introduced, old stations retired or station maintenance.

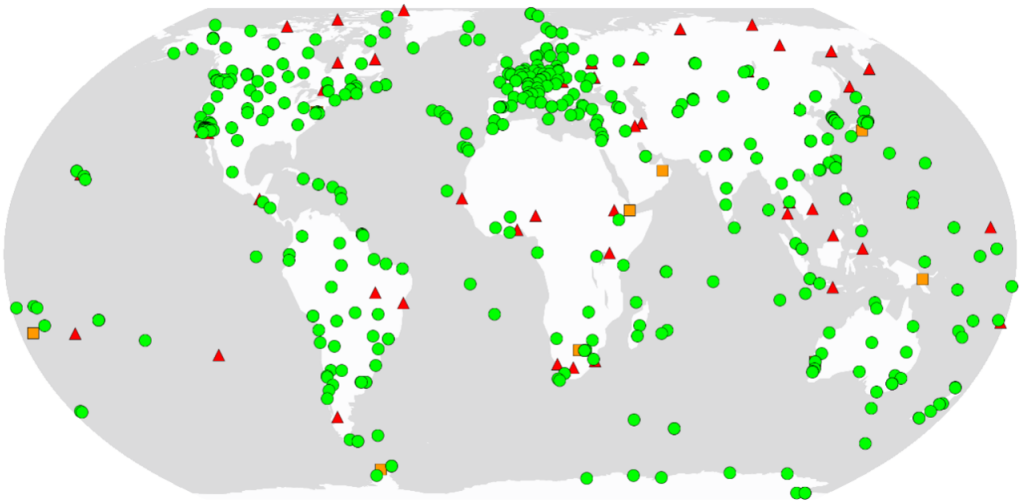

Figure 1: IGS Map and stations. IGS (2023)

In this paper, we used GNSS measurements from IGS receivers and precise GNSS products, including precise ephemeris (.SP3 file), precise satellite clock bias (.CLK file), Differential Code Bias (.BIA file) and comparing the filter estimation with result from precise solution (.SNX file).

III. PPP BASIC

In this paper, the realization of PPP is an application of the Extended-Kalman Filter (EKF). It applies GNSS measurements to estimate user position and related information, such as receiver clock bias, tropospheric wet delay and carrier phase ambiguities. In addition to those factors that can be accuraly estimated by the filter, PPP also requires various correction models and external precise product to reduce the errors. Such products include precise ephemeris, precise satellite clock bias, Differential Code Bias (DCB) and Antenna Phase Center (APC) offset. The combined estimation gives centimeter-level accuracy for static receiver and decimeter-level for kinematic receiver.

A typical static PPP receiver can define its state as follows:

$$\overrightarrow{x} = \begin{bmatrix} x \\ y \\ z \\ b \\ \nabla b \\ \nabla \hat{T} \\ A^{(1)} \\ \vdots \\ A^{(k)} \end{bmatrix} \tag{1}$$

where $\overrightarrow{x}$ is the state of the static PPP filter that contains all the information needed for the estimation. x, y, z are the receiver position in Earth Centered Earth Fixed (ECEF) coordinate, b is the receiver clock bias, ∇b is the clock drift, which is the rate of change of receiver clock bias, $\nabla \hat{T}$ is the tropospheric wet delay offset in zentih direction, $A^{(k)}$ is the float ambiguities of k^{th} carrier phase measurement.

The propagation model and time-update for the state is straightforward for static receiver, they are identical except for the receiver clock bias where the clock drift take place.

$$\overrightarrow{x}_{t+1} = \begin{bmatrix} 1 & 0 & 0 & 0 & 0 & 0 & 0 & \dots \\ 0 & 1 & 0 & 0 & 0 & 0 & 0 & \dots \\ 0 & 0 & 1 & 0 & 0 & 0 & 0 & \dots \\ 0 & 0 & 0 & 1 & dt & 0 & 0 & \dots \\ 0 & 0 & 0 & 0 & 1 & 0 & 0 & \dots \\ 0 & 0 & 0 & 0 & 0 & 1 & 0 & \dots \\ \vdots & \vdots & \vdots & \vdots & \vdots & \vdots & \ddots & \vdots \\ 0 & 0 & 0 & 0 & 0 & 0 & 0 & 1 \end{bmatrix} \cdot \overrightarrow{x}_t \tag{2}$$

where dt is the discretized time interval.

The measurements used in the PPP filter are dual-frequency code phase and carrier phase pseudorange. Since the ionospheric delay is a frequency dependent, the dual-frequency measures can effectively reduce and almost eliminate such delay, making the duel-frequency measurements ionospheric-free.

The Iono-Free measurement models are defined as follow:

$$\rho_{\text{IF}}^{(i)} = \| \overrightarrow{x}_s^{(j)} - \overrightarrow{x}_{rx} \| + \left(b - b_s^{(i)} \right) + m^{(i)} \nabla \hat{T} + R_m + \epsilon^{(i)} \tag{3}$$

$$\phi_{\text{IF}}^{(i)} = \| \overrightarrow{x}_s^{(j)} - \overrightarrow{x}_{rx} \| + \left(b - b_s^{(i)} \right) + m^{(i)} \nabla \hat{T} + A^{(i)} + R_m + \epsilon^{(i)} \tag{4}$$

where $\rho_{\text{IF}}^{(i)}$ is the ionospheric-free code phase measurement, i represents i$^{\text{th}}$ measurement, $\overrightarrow{x}_s^{(j)}$ is the satellite position from ephemeris data, j represents j$^{\text{th}}$ satellite, $b_s^{(i)}$ is the satellite clock bias, $m^{(i)}$ is the mapping function of tropospheric delay error and ϵ is the un-modelled effects. $\phi_{\text{IF}}^{(i)}$ is the carrier phase ionospheric-free measurement. R_m consists all the modelled effects for both code and carrier phase, which include satellite antenna phase center offset, relativistic effects, solid earth tide modeling, ocean loading, modeled tropospheric delay, earth rotation travel correction(Sagnac Effect), phase wind up for carrier phase measurements and differential code bias. Notice the ionospheric-free measurements are computed from dual-frequency measurements, and no single frequency measurements are used in the estimation, so no ionospheric delay model is required, and all terms are converted to meter. This formulation does not consider the effect of multi-path error.

We verify the performance of such PPP formulation with GPS measurement from JPLM station on Sep.12th 2021.

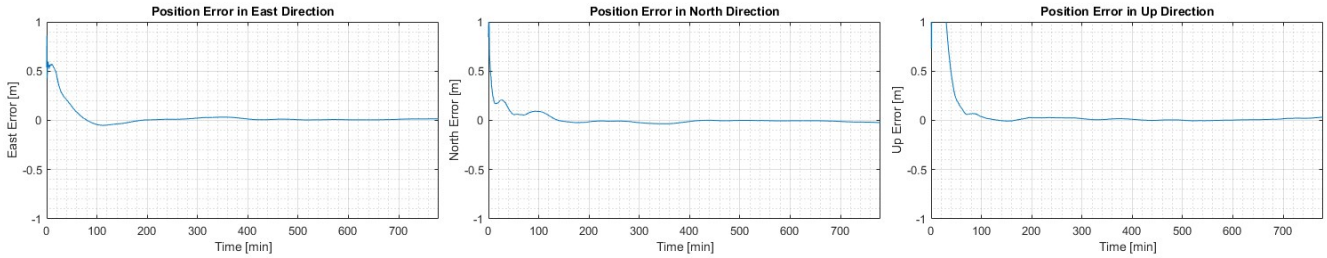

Figure 2: Position error in East-North-Up direction.

Fig.2 is the position difference between the filter and the solution from the Sinex file.

IV. PPP FAULT DETECTION

While the PPP filter can achieve centimeter accuracy, the filter itself is highly susceptible to any GPS fault. The Markovian process of EKF also makes it difficult to remove the effect of faults even after the presence of such fault. As a result, a PPP filter that can reflect the appearance of GPS faults and still tolerant to the impact of such fault is desired.

1. The Detection State

An additional state, the detection state ζ, is added to the original definition of state.

$$\overrightarrow{x} = \begin{bmatrix} x \\ y \\ z \\ b \\ \nabla b \\ \nabla \hat{T} \\ \zeta \\ A^{(1)} \\ \vdots \\ A^{(k)} \end{bmatrix} \tag{5}$$

ζ represents a free state that detect any error left from the PPP filter. It resets to zero in the time update, and has high process noise, meaning this state only reflects the error from measurement update.

$$\rho_{\text{IF}}^{(i)} = \| \overrightarrow{x}_s^{(j)} - \overrightarrow{x}_{rx} \| + \left(b - b_s^{(i)} \right) + m^{(i)} \nabla \hat{T} + R_m + \zeta + \epsilon^{(i)} \tag{6}$$

$$\phi_{\text{IF}}^{(i)} = \| \overrightarrow{x}_s^{(j)} - \overrightarrow{x}_{rx} \| + \left(b - b_s^{(i)} \right) + m^{(i)} \nabla \hat{T} + A^{(i)} + R_m + \zeta + \epsilon^{(i)} \tag{7}$$

Eq.(6) and Eq.(7) are the new measurement models with detection state ζ.

2. Monitoring the Satellite Clock Fault

In order to monitor the satellite clock fault, the detection state is placed at the designated measurements of satellite of choice. For instance, to monitor the satellite clock of Pseudo-Random Noise (PRN) 1 GPS satellite, the detection state is put to the measurement models of the entire PRN 1, since a satellite clock bias equally affect all the measurements from that satellite. The

corresponding observation matrix $\mathbf{C}$ is thus:

$$\mathbf{C} = \begin{bmatrix} -\mathbf{1}^{(1)} & 1 & 0 & m^{(1)} & 1 & 0 & 0 & 0 & \dots \\ -\mathbf{1}^{(2)} & 1 & 0 & m^{(2)} & 0 & 0 & 0 & 0 & \dots \\ -\mathbf{1}^{(3)} & 1 & 0 & m^{(3)} & 0 & 0 & 0 & 0 & \dots \\ -\mathbf{1}^{(1)} & 1 & 0 & m^{(1)} & 1 & 1 & 0 & 0 & \dots \\ -\mathbf{1}^{(2)} & 1 & 0 & m^{(2)} & 0 & 0 & 1 & 0 & \dots \\ -\mathbf{1}^{(3)} & 1 & 0 & m^{(3)} & 0 & 0 & 0 & 1 & \dots \\ \vdots & \vdots & \vdots & \vdots & \vdots & \vdots & \vdots & \vdots & \vdots \end{bmatrix} \tag{8}$$

where $\mathbf{1}$ is light-of-sight directional vector pointed from the estimated receiver to the corresponding satellites. They varies from satellites to satellites. $\mathbf{C}$ is the Jacobian matrix of measurement models Eq.(6) and Eq.(7). The detection state ζ is always presented on the measurements from PRN 1 which forms a one-vector in $\mathbf{C}$ for detection state and PRN 1 measurements.

3. Impact of Detection State

The addition of detection state does not come without cost to the system. The detection state effectively reduces the redundancy of the available satellites. Notice the measurement model of EKF is:

$$\overrightarrow{y} = \mathbf{C} \cdot \overrightarrow{x} \tag{9}$$

which is equivalent to

$$\overrightarrow{y} = \begin{bmatrix} -\mathbf{1}^{(1)} & 1 & 0 & m^{(1)} & 1 & 0 & 0 & 0 & \dots \\ -\mathbf{1}^{(2)} & 1 & 0 & m^{(2)} & 0 & 0 & 0 & 0 & \dots \\ -\mathbf{1}^{(3)} & 1 & 0 & m^{(3)} & 0 & 0 & 0 & 0 & \dots \\ -\mathbf{1}^{(1)} & 1 & 0 & m^{(1)} & 1 & 1 & 0 & 0 & \dots \\ -\mathbf{1}^{(2)} & 1 & 0 & m^{(2)} & 0 & 0 & 1 & 0 & \dots \\ -\mathbf{1}^{(3)} & 1 & 0 & m^{(3)} & 0 & 0 & 0 & 1 & \dots \\ \vdots & \vdots & \vdots & \vdots & \vdots & \vdots & \vdots & \vdots & \vdots \end{bmatrix} \cdot \begin{bmatrix} x \\ y \\ z \\ b \\ \nabla b \\ \nabla \hat{T} \\ \zeta \\ A^{(1)} \\ \vdots \\ A^{(k)} \end{bmatrix} \tag{10}$$

Since the detection state is always set to zero in the time-update, the value of detection state at measurement update is always zero.

$$\overrightarrow{y} = \begin{bmatrix} -\mathbf{1}^{(1)} & 1 & 0 & m^{(1)} & 1 & 0 & 0 & 0 & \dots \\ -\mathbf{1}^{(2)} & 1 & 0 & m^{(2)} & 0 & 0 & 0 & 0 & \dots \\ -\mathbf{1}^{(3)} & 1 & 0 & m^{(3)} & 0 & 0 & 0 & 0 & \dots \\ -\mathbf{1}^{(1)} & 1 & 0 & m^{(1)} & 1 & 1 & 0 & 0 & \dots \\ -\mathbf{1}^{(2)} & 1 & 0 & m^{(2)} & 0 & 0 & 1 & 0 & \dots \\ -\mathbf{1}^{(3)} & 1 & 0 & m^{(3)} & 0 & 0 & 0 & 1 & \dots \\ \vdots & \vdots & \vdots & \vdots & \vdots & \vdots & \vdots & \vdots & \vdots \end{bmatrix} \cdot \begin{bmatrix} x \\ y \\ z \\ b \\ \nabla b \\ \nabla \hat{T} \\ \zeta = 0 \\ A^{(1)} \\ \vdots \\ A^{(k)} \end{bmatrix} \tag{11}$$

As a result, the column-wise manipulation of detection state makes no difference to the expected measurement, and the resulting measurement model is:

$$\overrightarrow{y} = \begin{bmatrix} \mathbf{0}^{(1)} & 0 & 0 & 0 & 1 & 0 & 0 & 0 & \dots \\ -\mathbf{1}^{(2)} & 1 & 0 & m^{(2)} & 0 & 0 & 0 & 0 & \dots \\ -\mathbf{1}^{(3)} & 1 & 0 & m^{(3)} & 0 & 0 & 0 & 0 & \dots \\ \mathbf{0}^{(1)} & 0 & 0 & 0 & 1 & 1 & 0 & 0 & \dots \\ -\mathbf{1}^{(2)} & 1 & 0 & m^{(2)} & 0 & 0 & 1 & 0 & \dots \\ -\mathbf{1}^{(3)} & 1 & 0 & m^{(3)} & 0 & 0 & 0 & 1 & \dots \\ \vdots & \vdots & \vdots & \vdots & \vdots & \vdots & \vdots & \vdots & \vdots \end{bmatrix} \cdot \begin{bmatrix} x \\ y \\ z \\ b \\ \nabla b \\ \nabla \hat{T} \\ \zeta = 0 \\ A^{(1)} \\ \vdots \\ A^{(k)} \end{bmatrix} \tag{12}$$

where the light-of-sight vector, clock bias, and tropospheric wet delay of PRN 1 is zero. It indicates that the addition of detection state to PRN 1 is equivalent to excluding PRN 1 from the estimation of the filter position, clock bias and tropospheric wet delay.

V. ARTIFICIAL FAULT RESULT

Two types of faults are injected to the IGS observation data, step fault and ramp fault, to evaluate the ability of fault monitoring.

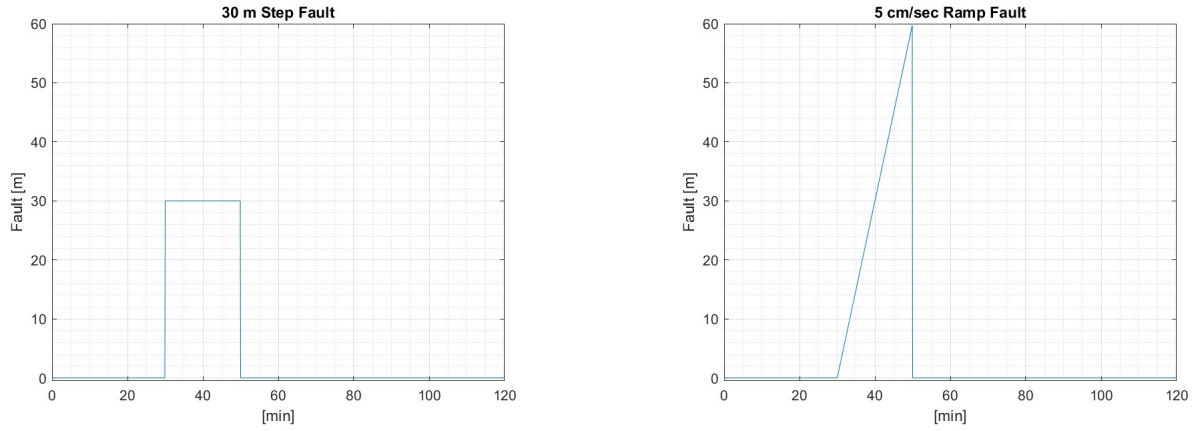

(a) 30 meters Step Fault

(b) 5 cm/sec Ramp Fault

Figure 3: Fault injection types.

The step and ramp faults in Fig.3a and Fig.3b begin at 30 min and end at 50 min. The step fault has magnitude of 30 m and ramp fault has fault rate at 5 cm/sec.

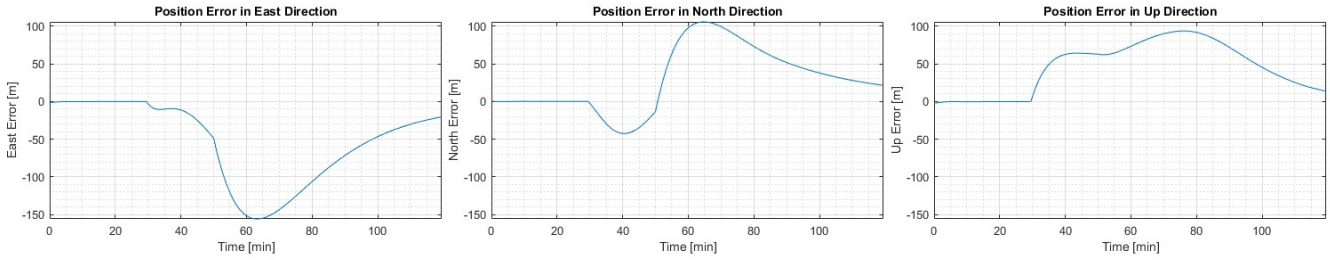

Figure 4: Position error in East-North-Up direction with step fault.

Fig.4 is the position error of JPLM station on Sep.12$^{\text{th}}$ 2021 when the step fault from Fig.3a is injected to PRN 1. In other

words, for JPLM station there is a 30 m step satellite clock fault occurs on PRN 1 from 30 to 50 minutes of the day. We can see the 30 m satellite clock fault causes a significant impact in the position domain, leading to as much as 150 meters of error in any direction. In addition, the impact of fault does not disappear immediately after the end of fault. It takes more time than the presence of fault to recover. In this case, restarting the filter is a better choice.

By adding detection state ζ to PRN 1, such satellite clock fault can be detected and therefore protect the filter.

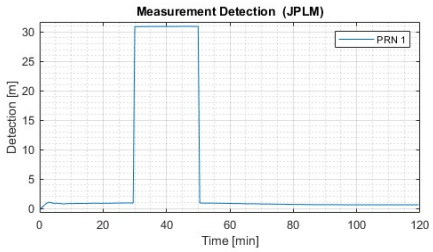

Figure 5: Detection state with step fault injection

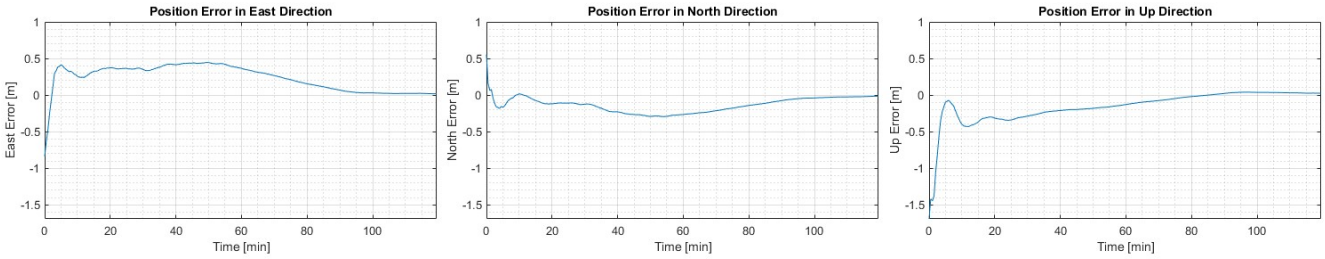

Figure 6: Position error in East-North-Up direction with detection state and step fault.

Fig.5 is the value of detection state. When the 30 m step clock fault occurs on PRN 1 from 30 to 50 min of time, we can see the detection state captures the onset and termination of the step fault. Fig.6 is the position error of the filter and its unaffected by the step fault.

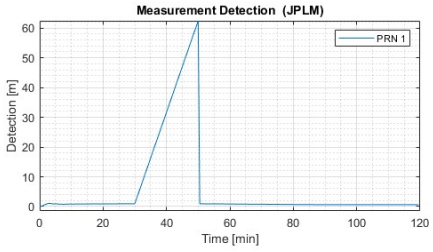

Figure 7: Detection state with ramp fault injection

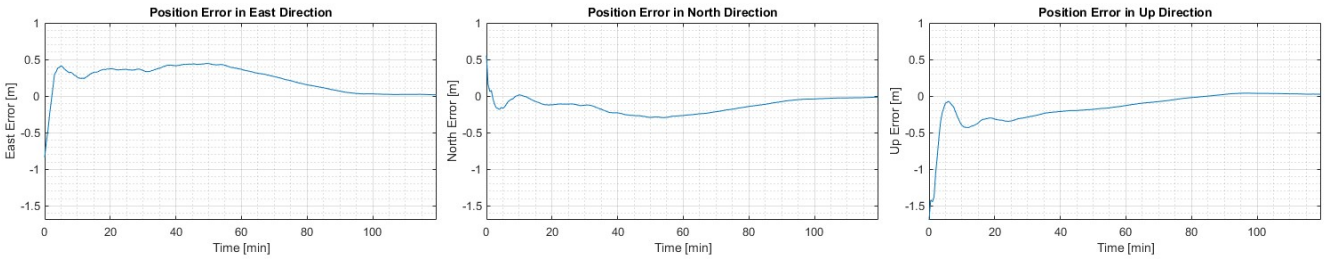

Figure 8: Position error in East-North-Up direction with detection state and step fault.

Similarly, the 5 cm ramp fault is also successfully detected. Fig.7 is the value of detection state monitoring PRN 1. Fig.8 is the position error under the ramp fault, and its the same as Fig.6.

VI. ACTUAL FAULT RESULT

GPS PRN-1 (SVN-63) has experienced several clock faults and anomalies in 2023. Particularly, there was a step fault occurred on GPS PRN-1 on Jan. 25th, an anomaly on Jan. 28th and a ramp fault on July 10th. Due to SVN-63 demonstrating unpredictable performance and operating on its last clock, it was retired on Aug. 10th and SVN-44 was reactivated and operates under PRN-22 as the replacement to PRN-1.

1. Jan. 25th Fault

The fault happened on Jan. 25th when PRN-1 was over in the middle of South Pacific, so the data collected by the nearby station, GAMB, located in Gambier, French Polynesia, is selected to analyze the fault.

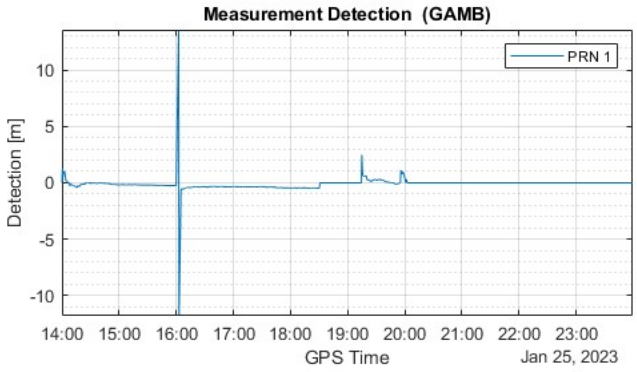

Figure 9: Detection state value on Jan. 25th.

Fig.9 is the value of the detection state that a fault-tolerant filter monitors PRN-1 using the measurements from GAMB station on Jan 25th. There are impulse responses at 16:00:00 on that day, indicating the onset of the fault, but it quickly recovered after 16:02:30 and remain relatively low until PRN-1 is out of view. It appears that no fault occurred on PRN-1 on Jan. 25th. The reason for having this normal behavior of the detection state is because the precise satellite clock product used by the filter was release several weeks after the incident, and the fault had been identified and corrected in the precise product. Therefore, the fault is hidden in the precise product.

To replay the fault as it happened, in stead of the precise satellite clock bias product, we apply the satellite clock bias from the navigation message (BRDC file) that was broadcast during the fault period. This would inevitably degrade the accuracy of the filter since the clock bias is not ”precise” and the accuracy is no longer to the PPP standard, but this would allow the fault to appear in the estimation. In real practice, the precise product is computed and broadcast to the user in real-time so the fault would still exist in such precise products.

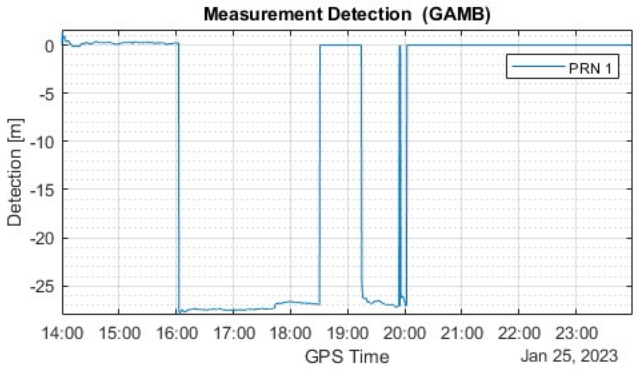

Figure 10: Detection state value on Jan. 25th.

Fig.10 is the value of the detection state from the same filter, but the broadcast satellite clock bias from the navigation message is used rather than the precise product. The fault represented by the detection state is consistent with the fault analyzed in Wang and Walter (2023), The only difference is it begins few minutes earlier, at 16:02:30, when the detection state drops to around -27 m, then persists until 18:30:30. From 18:31:00 to 19:14:30 the measurements from PRN-1 is missing due to the satellite being switched to non-standard code, and then the signal is received again after 19:15:00 and labelled unhealthy. The users were exposed to faulted GPS PRN-1 signal for up to 3.5 hours after 16:00:00 on Jan 25th, which threatened the integrity of the user if the measurements from PRN-1 had been used in the position estimation.

The evolution of the value of the detection state from the fault-tolerant filter gives the real-time estimation of any abnormal behavior of the satellite clock or corrections that are monitored by the filter. It shows that the fault-tolerant filter can detect not only the artificial but also actual clock faults as they occurred in real-time. The detection state can replicate the pseudorange error induced by the satellite clock, so one only has to look at the detection state to monitor the fault events.

2. Jan. 28th Anomaly

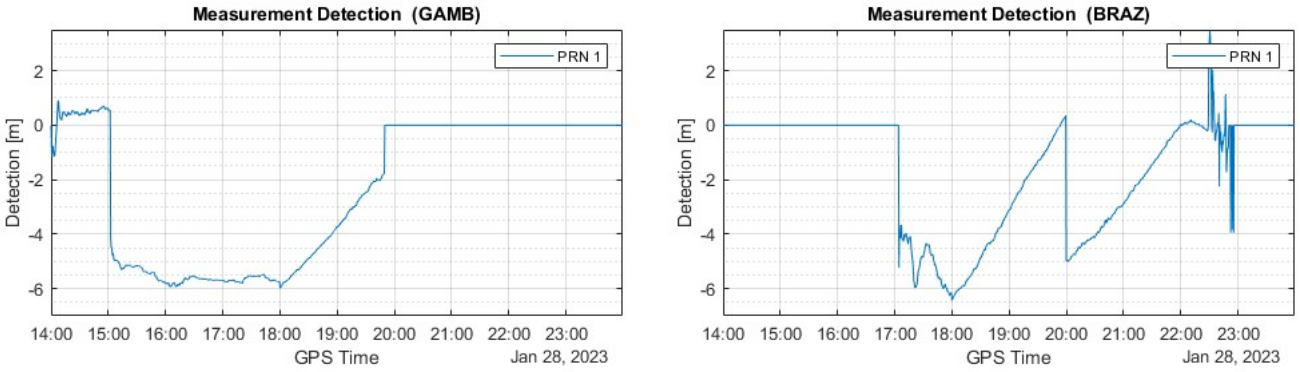

(a) Detection state value on Jan. 28th at GAMB

(b) Detection state value on Jan. 28th at BRAZ

Figure 11: GPS PRN-1 anomaly on Jan. 28th.

Fig.11a and 11b are the value of the detection states from GAMB and BRAZ stations respectively. Due to the lengthy persistence of the anomaly that happened on PRN-1 on this day, single station could not maintain line-of-sight to PRN-1 from the start to the end of the anomaly, so two stations, GAMB and BRAZ, are introduced into the analysis of the anomaly event. In Fig.11a, the anomaly begins at 15:02:30 where the detection state drops to around -5 m and drops to -6 m. PRN-1 is set unhealthy at 16:05:00 so the 6 m step anomaly is exposed to the user for an hour. At 18:00:00, the clock anomaly begins to be corrected by manual control, causing the gradual increment of the detection state. The correction of the anomaly is completed at 20:00:00, but drops to -5 m immediately. The same correction process is repeated and the whole correction is accomplished at 22:00:00. The noisy disturbance appear after 23:30:00 at BRAZ is because of the low elevation angle cut-off.

3. July. 10th Fault

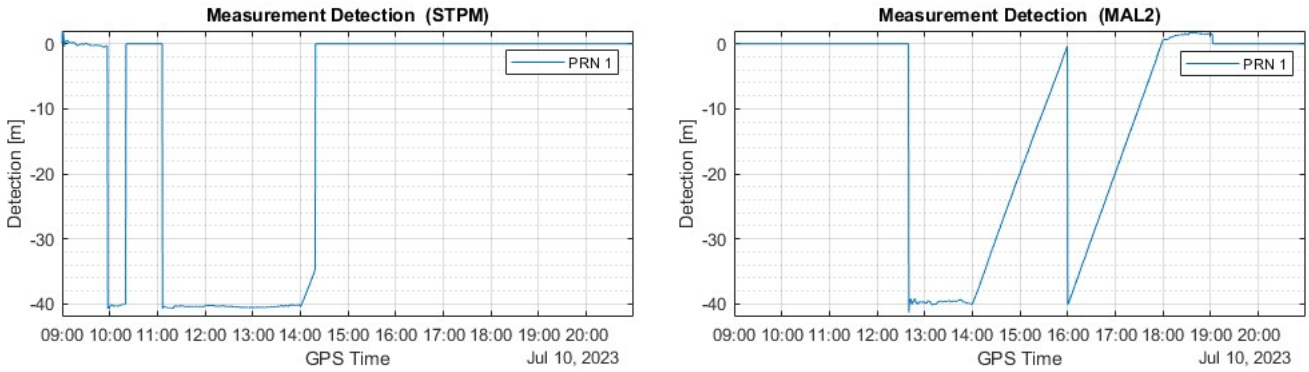

(a) Detection state value on July. 10th at STPM

(b) Detection state value on July. 10th at MAL2

Figure 12: GPS PRN-1 fault on July. 10th.

Similar to the anomaly event on Jan. 28th, the entire evolution of the July. 10th fault is too long to be recorded by single static receiver, so there are two stations, STPM and MAL2, being used in the analysis of the fault, which record the former and latter half of the fault respectively. Fig.12a and 12b are the value of the detection state from STPM and MAL2. They demonstrate that the fault begins at 09:57:00, when a -40 m step fault occurs. The fault is identified after 23 min and PRN-1 is changed to using Non-Standard Codes at 10:20:30, hence no measurements from PRN-1 are recorded, and is marked un-healthy after 11:06:00. The fault persists until 14:00:00 when the satellite clock is corrected manually. The detection state steadily increases with a constant rate to 0 at 16:00:00, but then immediately drops to -40 m again. The correction process repeats and the step fault is corrected at 19:00:00.

VII. FAULT MONITORING SYSTEM

It is demonstrated in Sec.V and VI that the fault-tolerant filter is capable of detecting the satellite clock faults in both the artificial and actual clock fault scenarios. Since the requirement of operating such fault-tolerant filter is no different than a standard PPP filter, the filter can be used in real-time at any of the PPP reference station or anywhere with access to the measurement data and precise product.

A simple fault monitoring system can be formulated as the fault-tolerant filter is the basis, with multiple fault-tolerant filters running in parallel and each of the filter is monitoring different satellites in-view. The following is an example of the operation of the fault monitoring. For a receiver with 7 satellites in-view, the monitoring system would establish 7 fault-tolerant filters and each of the filter has detection state corresponds to each satellite. In other words, the filters are applying 6 out of 7 line-of-sight information in the estimation of the filter state, and 1 in the additional satellite clock information the filter is monitoring. All 7 filters are running in parallel and the clock fault detection can be achieved with observing the evolution of the detection states.

There are 3 types of result for the fault-tolerant filter when considering only the single clock fault scenario.

1. Nominal: No fault is present in the satellites in-view, and all values of detection states are closed to zero.
2. Dedicated Fault: A clock fault happens on the satellite that is the detection state of the fault-tolerant filter is monitoring. For instance, a clock fault happens on PRN-1, and the fault-tolerant filter is also monitoring PRN-1.
3. Non-Dedicated Fault: A clock fault happens on the satellite that is not the detection state is monitoring. For example, when the a fault occurs on PRN-1, but the filter is monitoring PRN-5.

Nominal is when no fault is happening on any of the satellites in-view to the receiver, which should be the sate of all the filters in the majority of the time. When a fault occurs to the satellite in-view, since for the fault-monitoring system all satellites are at least monitored by one of the fault-tolerant filters, the Dedicated and Non-Dedicated faults are inevitable and will both occur at the same time. The focus is therefore distinguish between the Dedicated and Non-Dedicated faults based on the different reactions on the fault-tolerant filters.

The step fault happened on PRN-1 on Jan. 25th at GAMB station is studied as an investigation on the different impacts on the receiver for Dedicated and Non-Dedicated faults.

1. Dedicated Fault

The response of the detection state for the Dedicated Fault is exactly as Fig.10, where the step fault goes entirely into the detection state and all the other states, such as receiver clock bias, tropospheric wet delay and measurement residuals, are protected such that the values are within reasonable ranges. In other words, the filter experiencing Dedicated Fault should have all the states operate within their nominal error model.

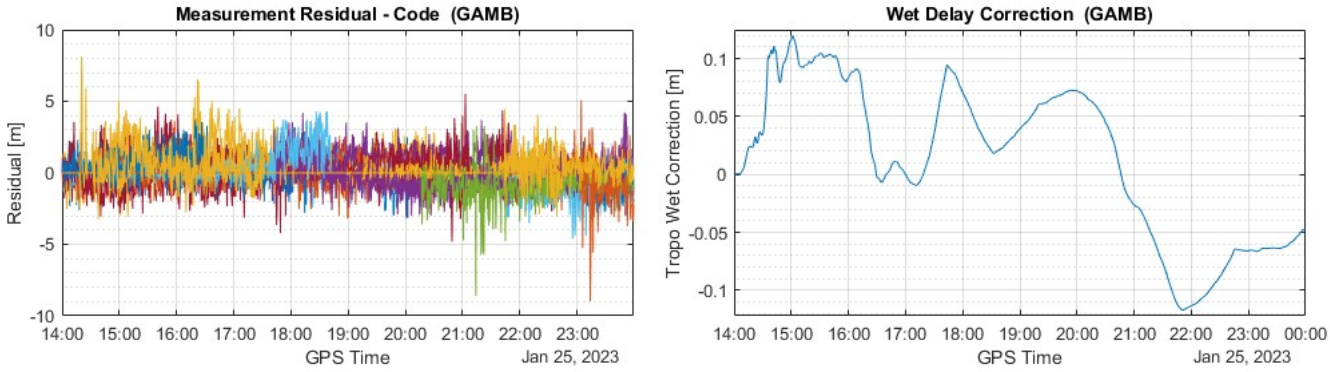

(a) Residual of Dedicated Code-Phase Measurements

(b) Dedicated Tropospheric Wet Delay Correction

Figure 13: Dedicated Fault.

As pointed out in Sec.IV.3, the addition of detection state to all the measurements from PRN-1 is effectively excluding the line-of-sight information from the estimation of all the states except for the carrier phase ambiguity of PRN-1. As a result, the Dedicated Fault would have no effects on all the other states, and they remain in normal operation. Fig.13a is the residuals of all the code-phase measurements. They exhibit the zero-mean and is as expected for normal code-phase measurements. Fig.13b is the estimated tropospheric wet delay correction, $\nabla\hat{T}$, and the value of the additional zenith wet delay correction to the tropospheric model is also within realistic range.

2. Non-Dedicated Fault

For Non-Dedicated Fault, the filter behavior is less predictable as the faulted line-of-sight information is used in the estimation of the filter state. This means the pseudorange error induced by the clock fault affects the state such as detection state, measurement residuals and tropospheric wet delay.

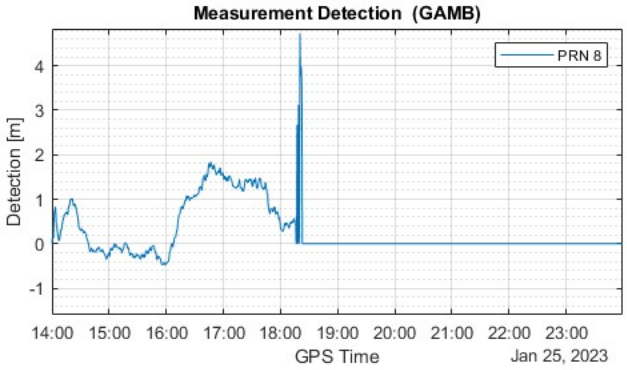

Figure 14: Non-Dedicated detection state value.

Fig.14 is the value of the detection state for a fault-tolerant filter monitoring PRN-8, where the fault happens on PRN-1. Recall the fault begins at 16:00:00 and as we can see the detection state of this filter rises after 16:00:00 and reaches 2 m at 16:45:00. It shows that the 27 m step fault on PRN-1 will change the detection state as well, regardless of which satellite the filter is monitoring.

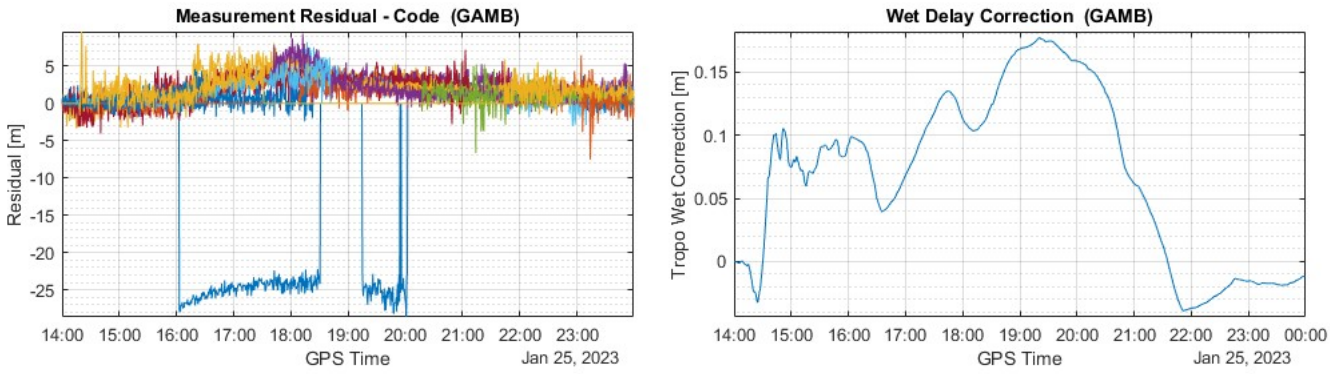

(a) Residual of Non-Dedicated Code-Phase Measurements

(b) Non-Dedicated Tropospheric Wet Delay Correction

Figure 15: Non-Dedicated Fault.

Fig.15a and 15b are the code-phase residuals and tropospheric wet delay correction of the fault-tolerant filter with Non-Dedicated fault. Unlike the Dedicated Fault where only the detection state responds to the step fault, all states, including the code-phase measurement residuals are influenced by the step fault. It is obvious that the residuals are reacting to the step fault, where the residual of the PRN-1 experiences a similar drop to the step fault itself, and the residuals of other satellites increase for a small amount, deviating from the zero-mean nominal value. The zenith wet delay of the filter is also different from the dedicated fault, with value reaching as much as 18 cm for zenith wet correction, which rarely happens in normal weather condition.

The distinct impact to the states of the fault-tolerant filter provides various possible ways of classifying between these two conditions. One can rely on comparing the detection state and the measurement residuals, or zenith wet delay correction. If detection state value exceeds a pre-defined threshold and the measurement residuals are not zero-mean distributed, then one can determine it is Non-Dedicated Fault. On the other hand if the residuals remain zero-mean distributed then it is Dedicated Fault. Similar process can be applied if the wet delay correction is chosen to be monitored. If both the detection state and the wet delay correction exceed certain thresholds then it is declared Non-Dedicated Fault.

However, in practice, it may be ambiguous basing on measurement residuals, wet delay correction or other states to determine the Dedicated and Non-Dedicated Fault. For single fault scenario, a simpler criteria is using only the magnitude of the detection states to decide the Dedicated and Non-Dedicated Fault. For Dedicated Fault, the pseudorange error would go entirely into the detection state and have no impact on the rest of the states in the filter. As for Non-Dedicated Fault, the error would affect not just the detection states but the entire filter. When the filer position is constrained with the true location, the change of states are not causing the magnitude of the detection state to be greater than the Dedicated Fault in general. In fact, since the EKF filter relies on the past estimation, the Non-Dedicated Fault can only change the states in a slower manner such that the Dedicated Fault will always have largest and fastest response to the clock fault. As a result, we propose by comparing the magnitude of the detection states to distinguish between Dedicated and Non-Dedicated faults. That is, in a fault event for all the detection states that have magnitudes exceed a pre-determined threshold, the one that has the largest magnitude is classified as Dedicated, and all the other filter are Non-Dedicated. This way we are able to obtain the faulted satellite from the fault-monitoring system.

Therefore, we can determine the fault condition of the filter with only the magnitude of the detection state.

1. Nominal: All detection states have magnitude below the threshold.
2. Dedicated Fault: At least one detection state has magnitude greater than the threshold, and the one with the largest magnitude reports Dedicated Fault.
3. Non-Dedicated Fault: All the other filters who also report fault events but have lesser detection state magnitude.

VIII. PROTOTYPE FAULT MONITORING

A prototype fault monitoring system is established by means of running a batch of fault-tolerant filters in parallel. The number of filters ran correspond to the number of satellites in-view, and detection states monitor each of the satellites per filter. The filter operates independently with the magnitude of the detection states reflect the monitoring outcome. There are 3 possible outcomes for the detecting results as described in Sec.VII, Nominal, Dedicated Fault and Non-Dedicated Fault.

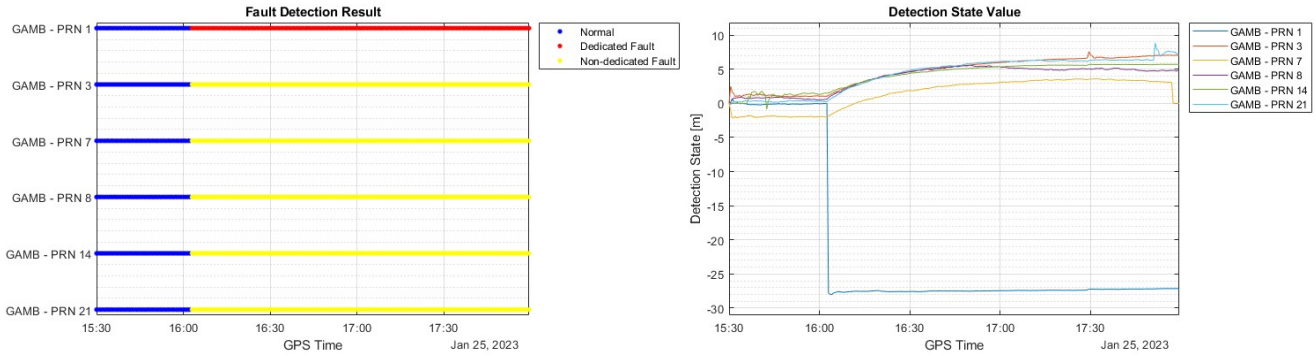

Figure 16: Monitoring results at GAMB stations on Jan. 25th

Fig.16 is the detection result of the prototype monitor using the measurements at GAMB station on Jan. 25th. There are 6 filters running in parallel with PRN-1, 3, 7, 8, 14 and 21 are monitored. The diagram on the left represents one of the three detection results of each filter. Blue indicates the filter is in Nominal condition, red is Dedicated Fault and yellow is Non-Dedicated Fault. It is shown that all filters report fault events after 16:02:30 and the filter monitoring PRN-1 has the Dedicated Fault, and all the other report Non-Dedicated Fault, which is consistent with the fact that the fault happened on PRN-1. The diagram on the right shows the values of the detection states. We can see the detection state monitoring PRN-1 has the largest magnitude. In contrast, the other detection states have much smaller magnitude and their responses are slower than the dedicated one. The reason for the sluggish growth of the Non-Dedicated filters is the pseudorange error, the step fault, affects not only the detection state but other states such as clock bias and wet delay, and since EKF relies on the past estimation of the filter state the detection state reflects the change of other states in the Non-Dedicated Fault so the detection state does not change as fast as the dedicated one. Because of this we can determine the Dedicated and Non-Dedicated fault based only on the magnitude of the detection states as expressed in the diagram on the right.

Similar results are obtained from faults occurred on Jan. 28th and July. 10th. The prototype fault-monitoring system identify PRN-1 as the faulted satellite in the events on these two days.

IX. CONCLUSION

We formulated a dual-frequency fault-tolerant PPP filter. It can achieve centimeter-level accuracy for static receivers. GPS observation data and precise correction products such as precise ephemeris, precise satellite clock bias, DCB and APC offset from IGS are used to evaluate and simulate the performance of the PPP filter. It is shown that PPP is susceptible to satellite clock faults, and a single clock fault on a satellite can cause even larger errors in the position domain. It also takes significantly more time for the filter to recover from fault. We added an extra state to the filter, called detection state, that can protect the filter and detect the GPS fault, particularly the satellite clock fault. Adding a detection state to the filter for satellite clock fault monitoring is effectively excluding the monitored satellite from the state estimation, so the number of faults a filter can cover depends on the redundancy of the GNSS satellites. It is demonstrated the fault-tolerant filter can detect the artificial and actual clock faults. This paper evaluates the GPS clock faults that happened on Jan. 25th, Jan. 28th and July. 10th with the fault-tolerant filter using the broadcast satellite clock bias. Finally, a prototype monitoring system is established with the fault-tolerant filter as the basis components to its operation. The magnitude of the detection state is used to verify the fault categories, the Nominal, Dedicated Fault and Non-Dedicated Fault, and we have shown this classifying criteria successfully identify the faulted satellite in the actual clock fault events.

The next step for the fault-monitoring system is to include multiple satellites into one filter so as to reduce the number of filters required to run in parallel, and investigate the impact of multi-fault situations to the filters and the possibility of multi-constellation positioning to increase the redundancy of the filter. In addition, a more mathematically rigorous approached is needed for the nominal error bounding and obtaining threshold for the detection states.

ACKNOWLEDGEMENTS

We gratefully acknowledge the support of the Hexagon and NovAtel Inc. for funding this work. We also thank the FAA Satellite Navigation Team for funding this work under Memorandum of Agreement #: 693KA8-22-N-00015.

REFERENCES

Barrios, J., Pericacho, J. G., Calabrese, A., Fernández, G., Esteban, V. M., Fernández, M. Á., Bravo, F., Calle, J. D., Minaya, B. T., Figueiras, J. P., et al. (2020). Australia and new zealand sbas and ppp testbed: Achievements after three years of service. In *Proceedings of the 33rd International Technical Meeting of the Satellite Division of The Institute of Navigation (ION GNSS+ 2020)*, pages 1394–1432.

Blanch, J., Walker, T., Enge, P., Lee, Y., Pervan, B., Rippl, M., Spletter, A., and Kropp, V. (2015). Baseline advanced raim user algorithm and possible improvements. *IEEE Transactions on Aerospace and Electronic Systems*, 51(1):713–732.

Chen, K., Chang, G., and Chen, C. (2021). Ginav: A matlab-based software for the data processing and analysis of a gnss/ins integrated navigation system. *GPS Solutions*, 25(3):108.

Gunning, K., Blanch, J., Walter, T., de Groot, L., and Norman, L. (2018). Design and evaluation of integrity algorithms for ppp in kinematic applications. In *Proceedings of the 31st International Technical Meeting of the Satellite Division of The Institute of Navigation (ION GNSS+ 2018)*, pages 1910–1939.

IGS, M. (2023). International gnss service.

Mervart, L., Lukes, Z., and Alves, P. (2022). Terrastar x technology: Design of gnss corrections for instantaneous lane-level accuracy on large scale connected vehicles and devices. In *Proceedings of the 35th International Technical Meeting of the Satellite Division of The Institute of Navigation (ION GNSS+ 2022)*, pages 1280–1292.

Wang, R. and Walter, T. (2023). Characterization and comparison of galileo and gps anomalies. In *Proceedings of the 2023 International Technical Meeting of The Institute of Navigation*, pages 597–610.